This is the accepted manuscript made available via CHORUS. The article has been published as:

Synthetic helicoidal rotation of a quasielectrostatic ring resonator for ultrabroadband magnet-free nonreciprocity

Aravind Nagulu, Ahmed Mekawy, Mykhailo Tymchenko, Dimitrios Sounas, Harish Krishnaswamy, and Andrea Alù

Phys. Rev. Applied **22**, 064020 — Published 5 December 2024

DOI: 10.1103/PhysRevApplied.22.064020

Synthetic Helicoidal Rotation of a Quasi-Electrostatic Ring Resonator for Ultra-Broadband Magnet-Free Non-Reciprocity

Aravind Nagulu[1], Ahmed Mekawy[5], Mykhailo Tymchenko,[2] Dimitrios Sounas,[3] Harish Krishaswamy[4,*], and Andrea Alù[2,5,6,*]

[1]*Department of Electrical and Systems Engineering, Washington University in St. Louis, St. Louis MO 63130, USA*

[2]*Department of Electrical & Computer Engineering, The University of Texas at Austin, Austin, TX 78712, USA*

[3]*Department of Electrical Engineering, Wayne State University, Detroit, MI 48202, USA*

[4]*Department of Electrical Engineering, Columbia University, New York, NY 10027, USA*

[5]*Photonics Initiative, Advanced Science Research Center, City University of New York, New York, NY 10031, USA*

[6]*Physics Program, Graduate Center, City University of New York, New York, NY 10016, USA*

[*]To whom correspondence should be addressed (email: harish@ee.columbia.edu, aalu@gc.cuny.edu)

Suitably tailored forms of spatio-temporal modulation in electronic circuit networks have been recently employed to overcome fundamental challenges in modern electronic systems, including breaking reciprocity, squeezing the footprint of high-Q resonators, and overcoming the delay-bandwidth limit. Rotating patterns of temporal modulations have been used to synthesize angular momentum, which replaces magnetic bias to break reciprocity in integrated circuits. However, this approach is limited by trade-offs between modulation speed, footprint and bandwidth of operation. Rotating switching patterns in commutated capacitor networks also enable compact filters and quasi-electrostatic wave propagation overcoming the delay-bandwidth limit. In this

paper, we combine these mechanisms in an integrated circuit ring that synthetically rotates in two dimensions, realizing an effective helicoidal motion that provides ultra-broadband quasi-electrostatic non-reciprocal responses fitting within a theoretically infinitesimal size. We also analyze the impact of modulation signal noise on time-modulated non-reciprocal components and unveil the role of a dynamic noise mechanism based on which the noise level increases in the presence of a strong signal passing through the component, along with methods to mitigate this effect. We experimentally verify these principles in a 3-port integrated circulator based on a 65nm CMOS process that operates from DC to 1GHz with a miniaturization factor of 2×10^6.

Introduction

Devices with non-reciprocal transmission are common in microwave communications, and radar/imaging sensors [1]. The traditional approach to realize these functionalities is to use ferrite materials biased by an external magnetic field. Unfortunately, such materials are not compatible with existing semiconductor manufacturing processes, leading to large size and high implementation costs. Approaches to achieve magnet-free non-reciprocity include active voltage-/current- biased transistors [1]- [6]. However, these approaches have found limited application due to their poor noise and linearity performance [6]. Non-linearity in circuits or materials can also be exploited to achieve non-reciprocity [7]-[13]. However, these devices typically exhibit non-reciprocal responses across a limited range of signal power and introduce distortions in the transmitted signals, thereby restricting their application. Recent research has investigated the possibility of low-noise and linear magnet-free non-reciprocity through parametric phenomena enabled by spatio-temporal modulation across several physical domains, including acoustics, microwave electronics and optics [14]-[19]. Approaches based on time modulation typically rely on forms of synthetic motion of a circuit or material platform achieved through carefully

engineered patterns of spatio-temporal modulation that synthesize linear or angular momentum, taking inspiration from the fact that wave propagation in moving media is non-reciprocal. For instance, the rotary motion of air within an acoustic ring cavity was shown to enable non-reciprocity for sound waves through angular-momentum biasing [20]. Synthetic rotary motion to realize angular-momentum biasing through traveling-wave modulation of a ring cavity has been used to demonstrate non-reciprocal circulators at optical [21] and microwave frequencies, either in all-electronic systems [22]-[24] or in hybrid acoustic-electronic systems [25]-[27]. Similarly, synthetic rotary commutation across a bank of capacitors or delay lines has also been used to enable non-reciprocity at microwaves in [28]-[34]. Linear momentum biasing through synthetic motion along a linear axis imparted by traveling-wave modulation along a waveguide or transmission line has also enabled non-reciprocity at optical [35]-[38] and microwave [39]-[41] frequencies. Several other interesting non-reciprocal phenomena such as non-reciprocal antennas [42],[43], non-reciprocal metasurfaces [44],[45], and non-reciprocal topological insulators [46],[47] have been demonstrated based on time-modulated synthetic motion.

While promising, these approaches have all shown a fundamental trade-off between footprint, bandwidth and modulation speeds. Linear momentum biasing must be performed along distances that are inversely proportional to the modulation strength. At microwave frequencies, variable capacitors (varactors) can tune over capacitance ratios of 2-4, leading to implementations that are in the order of one wavelength in size [39]. Alternatively, angular momentum biasing in a resonant ring eliminates frequency conversion, and the resonance miniaturizes the size to sub-wavelength dimensions, but this is associated with a reduction in the bandwidth of operation [19].

In a different context, commutated networks of capacitors have been shown to realize *quasi-electrostatic* comb filters, commonly called *N-path filters*, that do not require inductors,

hence leading to unprecedented form factors for sharp filtering responses [48],[49]. More recently, commutated networks of capacitors operating in a different *slow-wave* regime have been shown to support *quasi-electrostatic* wave propagation beyond the delay-bandwidth limit, leading to ultra-wideband phase delays within very compact footprints [50]. Also in these cases, a rotating modulation pattern is key: by synthetically rotating two arrays of switches at the input and output ports of the device, the input signal is first temporarily stored in a capacitor bank connecting the two ports, and then released to the output port with an arbitrary delay, over a bandwidth only limited by the Nyquist-Shannon sampling theorem [52].

In this paper, we combine these functionalities in an ultra-compact ring circuit that synthetically rotates in two dimensions to (i) synthesize a quasi-electrostatic, frequency-independent, ring resonance in an ultra-compact volume, and (ii) synthetically spin it in order to efficiently break reciprocity. The result is a helicoidally-rotating ultra-compact circuit that overcomes the fundamental trade-offs between size and bandwidth, realizing unprecedented performance metrics for magnet-free non-reciprocity. Our experiments unveil a new form of magnet-free non-reciprocity, inherently *quasi-electrostatic* in nature, in which the electromagnetic energy, *independent of the frequency of excitation*, is dominantly stored in electric form, as opposed to systems that store energy dynamically in electric and magnetic fields in a series of resonators. Given its quasi-electrostatic nature, the non-reciprocal response of the circuit is observed over an extremely wide bandwidth, extending from DC to a cut-off frequency only limited by the specific technological implementation. The quasi-electrostatic nature also results in a circulator device with a theoretically infinitesimal footprint.

While non-reciprocal components based on parametric phenomena are theoretically noise free, the *phase noise* of the modulation signal can have detrimental impact on the functionality,

yet so far this issue has received little to no attention in the literature. As a second important objective of this work, we then explore a *dynamic noise mechanism* impacting its operation, as one example of several other non-reciprocal devices based on temporal modulations. We show that the phase noise of the modulation signal can transfer to the signal path in the presence of a strong signal passing through the component, and we introduce design guidelines that mitigate this effect. These results, broadly applicable to all classes of time-modulated non-reciprocal components, are critical to achieve the challenging noise metrics required in practical applications. We verify our findings through the experimental realization of a 3-port helicoidally-rotating quasi-electrostatic integrated-circuit circulator in a 65nm CMOS process that operates from DC to 1GHz with a miniaturization factor (defined as $\lambda^2/Area$) of 2×10^6.

I. Principle of Operation

Non-reciprocal transitions in systems bearing dynamic modulation are typically resonant [18], which implies a trade-off between bandwidth, modulation speed and footprint [30],[53]. Increasing the size of the device in favor of broadband non-reciprocal phenomena [54],[55] implies challenges in practical implementations, because the bandwidth and amplitude of modulation are inversely proportional [18],[35]. To alleviate the aforementioned trade-offs, we can consider non-resonant transitions to realize non-reciprocity, leveraging the recently introduced concept of quasi-electrostatic wave propagation [50], which also stems from suitably tailored temporal modulation schemes. Unlike wave propagation in normal media, in which the wave travels by periodically exchanging magnetic and electric stored energies in time, quasi-electrostatic wave propagation stores most of the energy in electric form, and synthetically moves it using temporal modulation in suitably designed circuit networks. The resilience of signal propagation in this form enables unprecedented features, especially in the context of broadband true-time-delay lines that overcome

the delay-bandwidth limit [57],[58]. The size of devices based on quasi-electrostatic propagation may become extremely small, while offering a broadband response, since storing electric energy is extremely efficient, as capacitors and switches can be miniaturized to an almost infinitesimal form factor. In this work, we leverage quasi-electrostatic wave propagation by synthetically rotating banks of capacitors in one dimension, and then rotate the system in another spatial dimension to impart angular momentum biasing and introduce broadband non-reciprocal routing.

As a first step to implement our device, we implement an electrostatic *frequency-independent* ring resonator. We realize this functionality by extending the concept of an N-path filter [48],[49] shown in Fig. 1a, a basic commutated network that has recently been used to synthesize filtering responses at radio frequencies in a compact footprint, but operating it in the *slow-wave* regime [50] to realize broadband responses. Its geometry consists of *N* identical capacitors of capacitance C placed between two ports, 1 and 2. The capacitors rotate in the vertical plane (see Fig. 1a) with angular frequency $\omega_s = \frac{2\pi}{T_s}$. At any given time, one capacitor is connected to port 1 and samples the input signal. Similarly, port 2 is placed at a staggered position, causing at any instant in time a different capacitor to be connected to port 2, and release its stored charge to the output port. Through the rotation, these capacitors remain connected to the ports for a time of T_s/N. Fig. 1a shows the scattering parameters of this device for two different scenarios. In the *filtering regime*, where the capacitors C are very large and the time constant $\tau = Z_0 C$ (Z_0 being the port impedance) is much larger than the switch ON time, $\tau \gg \frac{T_s}{N}$, the capacitors average the incident voltage at port 1 and transmit it to port 2, resulting in high-Q transmission peaks located at integer multiples of the rotation frequency ω_s, as shown in the bottom panel of Fig. 1a where $T_s/N\tau$ = 1/9. This comb-like frequency response is somewhat analogous to the one of a ring resonator, but with a much

reduced footprint, since the resonance is not supported by a geometrical factor (length of the ring compared to the wavelength), but simply by the modulation frequency, independent of its size. The absence of inductors in this geometry enables a drastic miniaturization. In addition, by suitably choosing the staggering of the ports, it is possible to implement a nonreciprocal phase response [56], offering the opportunity to realize compact but narrowband circulators [28] and gyrators [56]. On the other hand, in the *slow-wave regime*, when the capacitor value C is chosen so that $\tau \approx \frac{T_s}{N}$ [50], the capacitors can gracefully track the input voltage and discharge to the output port, so the sharp filtering response is lost and an electrostatic, *frequency-independent ring resonance* is achieved (bottom panel of Fig. 1a where $T_s/N\tau = 2$), confirming a broadband response extending from DC to a cut-off frequency determined by the time constant $1/\tau$.

Beyond the much-reduced footprint, there is another remarkable difference between this rotating structure and a conventional ring resonator: while a conventional ring supports degenerate right- and left-handed resonances because of symmetry, such a synthetically rotating circuit inherently selects only one handedness. To show this, we consider one capacitor of the circuit and spin it in the horizontal plane at angular frequency ω_s, thus connecting it sequentially to L ports $\leqslant$ N, as shown in Fig. 1b. The l^{th} port is located at angular position $\phi_l = \frac{2\pi l}{N}$, and each port is connected to the common capacitor for a period $\frac{T_s}{N}$. Interestingly, this rotation inherently enables a non-reciprocal response in the ring, by breaking the degeneracy in a way analogous to angular-momentum bias. Unlike a conventional ring resonator with degenerate clockwise (CW) and counter-clockwise (CCW) modes, the horizontal-plane rotation enables chiral circulation of the signals from one port to the next, following the mechanical rotation (CCW in Fig. 1b). This degeneracy lifting is at the basis of many implementations of non-reciprocal devices based on

angular momentum bias [21],[22] , and indeed it naturally implements non-reciprocal transmission. To prove this, we plot the scattering parameters of the circuit of Fig. 1b for $N = 8$ and $L = 3$ for two scenarios: $\frac{T_s}{N\tau} = \frac{1}{9}$ (filtering regime), and $\frac{T_s}{N\tau} = 2$ (slow-wave regime) as shown in the bottom panel of Fig. 1b. As expected, the scattering parameters are nonreciprocal. While the $T_s \ll N\tau$ scenario shows narrow peaks and large frequency selectivity, consistent with the conventional N-path filter response, for $\frac{T_s}{N\tau} = 2$, the nonreciprocal response is very broadband. Nevertheless, in both cases a large insertion loss is evident in Fig. 1b, stemming from the fact for that most of the time, namely $\frac{N-1}{N}T_s$ in each period, each port is disconnected from the circuit, and will experience an almost total reflection.

To overcome this problem, we combine the synthetic rotation in the horizontal plane (Fig. 1b) with the one in the vertical plane (Fig. 1a), and implement a circuit that synthetically rotates helicoidally (Fig. 1c). Since the vertical rotation enables ultra-broadband low insertion loss, and the horizontal rotation enables ultra-broadband non-reciprocal transmission, the helicoidal rotation is expected to realize a non-reciprocal ultra-broadband low-insertion-loss circulator. In Fig. 1c, we assume an implementation with $L = N$, and it is readily seen that the location of the active connections at any given time tracks a helical path due to the superimposed vertical-plane (Fig. 1a) and horizontal-plane (Fig. 1b) rotations. We plot the scattering parameters for this helicoidal rotation configuration for N=8 and L=3 in the bottom panel of Fig. 1c, showing, as expected, ultrabroadband, low-loss, non-reciprocal performance when $\frac{T_s}{N\tau} = 2$.

II. Theoretical Analysis

In order to rigorously analyze the helicoidally-rotating configuration, we consider a realistic electronic implementation of the synthetic motion of the capacitors through RF switches, as shown in Fig. 2a. Here we depict the case with the maximum number of ports that this electrostatic ring resonator can handle, $L = N$. This circuit consists of N identical layers connected in parallel to N ports, as shown in Fig. 2a. The switches in each layer are modulated in a revolving fashion so that only one switch in each layer is closed at any time (mimicking the horizontal-plane rotation of Fig. 1b, see the port staggering marked in the schematic in Fig. 2a). In addition, modulation of the switches in the parallel N layers are also staggered such that no two layers are connected to a port at the same time (mimicking the vertical-plane rotation of Fig. 1b, see the layer timing diagram sketched in Fig. 2a). As a whole, every port is connected to one of the N capacitors (say, at time $t=t_0$, the k^{th} capacitor C_k is connected to port $(k+p)\,\%\,N$, where % represents the modulo operation and $k,(p+1) \in 1,2,3..N$) and after a time T_s/N, the capacitors are connected to the subsequent ports (i.e., at time $t=t_0+T_s/N$, the k^{th} capacitor C_k is connected to $(k+p+1)\,\%\,N$ port), thus mimicking the helicoidal rotation depicted in Fig. 1c. Fig. 2b shows the evolution of the voltage on a capacitor across time. The capacitor is charged from one port (say port 1), and most of its charge is released to the next port (port 2). The left-over residue after this is discarded to subsequent ports (port 3, port 4, …). As we progress through the ports in the direction of the rotation, the residue becomes smaller thus leading to higher isolation. The addition of small matching inductors at the ports improves the circuit performance [50] by providing current boosting during both charging and discharging phases, thus improving the transmission to the subsequent port and increasing the isolation to other ports as shown by the green curve in Fig. 2b, and resulting in a *quasi-electrostatic* circuit. We stress that the size of these

inductors is much smaller than what would be required in a resonant implementation of an angular-momentum biased circulator, leading to much reduced footprints and much broader bandwidths. We performed a simulation for an 8-layer circulator with 8 ports for f_s = 500MHz, $\frac{T_s}{N\tau} = 2$, and the resulting scattering parameters are plotted in Fig. 2c. Building on our previous discussion, the scattering parameters show that the transmission loss S_{ij}, where $i = j + 1$, is wideband, and the isolation S_{kj} for any $k > j + 1$ keeps improving as k increases. Note that S_{81}=S_{12} from symmetry, and the large difference between S_{12} and S_{21} confirms the strong and wideband non-reciprocity. In practice, very high isolation levels beyond 40-50 dB are challenging to achieve because of parasitic coupling mechanisms, depending on the technology of implementation. In our CMOS implementation with 3 ports, the theoretical isolation is limited to 20-25dB.

In order to further quantify the scattering parameters based on the circuit parameters (τ, N, f_s), we analytically derived closed-form expressions for the expected scattering parameters for any number of layers N and any number of ports $L \leq N$ (the small matching inductors are neglected in this analytical formulation). We can write the scattering matrix as a function of the excitation frequency f in the limit $e^{-\frac{(L-1)T_s}{N\tau}} \ll 1$ as [51]

$$\left|S_{\beta\gamma}(\omega)\right| \approx \left|4\cos(\phi_0)\, \mathrm{e}^{(-\{(\beta-\gamma)\%L\}x)} \sin\left(\pi\left(\frac{\omega}{\omega_s N} - \frac{jx}{2\pi}\right)\right) sinc\left(\frac{\omega}{\omega_s N} - \frac{jx}{2\pi}\right)\right|, \qquad (1)$$

where β and γ represent the output and input ports and $\beta \neq \gamma$, $L \leq N$ represents the total number of ports, % represents the modulo operation, $\omega_S = 2\pi f_s = 2\pi/T_s$ is the angular frequency of modulation, $x = \frac{T_s}{N\tau}$, $\tau = Z_0 C$, $\mathrm{sinc}\, a = \sin \pi a\, /(\pi a)$ and $\phi_o = -\tan^{-1} \omega\tau$. It is obvious that the scattering matrix is not reciprocal as $S \neq S^T$.

We find that x, the ratio of switching time to charging and discharging times, plays a prominent role in determining the circulator response: for $x \ll 1$, we are in the filtering regime, where low insertion loss is seen over narrow bandwidths and we expect almost no non-reciprocity in transmission magnitudes. As we increase x into the slow-wave regime (e.g. x=2, corresponding to our implementation), the insertion loss increases only slightly (2.1dB at $f = f_s$ for x=2), but with a substantial increase in isolation (20dB at $f = f_s$ for x=2) and transmission bandwidth (a -3dB bandwidth of $2.2f_s$ for x=2). This can be seen in Fig. 2(d), where we plot the scattering parameters given by (1) at $f = f_s$ as a function of x for fixed number of layers $N = 8$, compared with full-wave circuit simulations [59]. As x increases even further, the insertion loss keeps increasing, as the discharge into the output port becomes more impulse-like. Anyhow, nonreciprocity is maintained over a very broad range of frequencies, and the isolation is found to be independent of frequency, hence resulting in an ultrawideband nonreciprocal response.

The bandwidth of the circulator increases with the number of layers *N* for fixed *x* and, in the limit $N \to \infty$, the circulator achieves low-loss transmission and high isolation across infinite bandwidth. This effect is quantified in Fig. 2(e) where we plot the device transmission (S_{21}) as a function of normalized frequency f/f_s, and number of layers N for *x*=2. The solid black contour line indicates that the -3dB bandwidth (defined as the frequency at which the S_{21} drops by 3dB from its maximum value) increases linearly with the number of layers *N*. The main penalty with increasing *N* is the challenge and complexity of generating *N* multiphase narrow clock pulses at the modulation frequency. The solid white circle in Fig. 2e represents our experiment, and is in good agreement with the measurement results shown in the next section.

This bandwidth enhancement can be understood by observing the synthetic rotation of the quasi-static ring. For very large *N*, the ring appears to be continuously rotating, so the capacitors are able to track the input signal effectively at every time instance. However, for small *N* the effective sampling frequency Nf_s is small, leading to a poor sampling efficiency of the incoming signal, thus leading to aliasing when the input frequency f is larger than the effective Nyquist rate $Nf_s/2$. In addition, the insertion loss for a fixed x and number of layers *N* can be further improved through small matching inductors in series with the ports, as discussed earlier and shown in the experimental section.

III. Noise in Time-Modulated Systems

Devices based on time modulation like the one introduced in the previous section are dependent on the timing accuracy of the modulation signals. While the effect of static timing errors in the modulation signals has been analyzed earlier [60],[61], the effect of random phase noise in the modulation signals is not well understood. In this scenario, a new dynamic noise mechanism emerges, where the phase noise interacts with a strong input signal to produce a signal-power dependent output noise, which results in a signal-strength dependent signal-to-noise ratio (SNR) degradation for other (weaker) signals that might co-exist with the strong input signal. While this mechanism is universal to all time-modulated non-reciprocal components, in our helicoidally rotating circulator, random fluctuations in the rising- and falling- clock edges result in uncertainty in the start and end of the charging phases, which consequently lead to an uncertainty of the voltage stored on the capacitor at the end of charging phase, V_c. This uncertainty in the capacitor voltage can be interpreted as an additional voltage noise $v_{c,noise}$ stored in the capacitor over and above the signal voltage in presence of no clock noise, $V_{c,o}$, i.e., $V_c = V_{c,o} + v_{c,noise}$ (see Fig. 3(a)). This voltage noise on the capacitor is directly proportional to the input voltage at the active port and the

amount of clock jitter. During the discharging phase, along with the signal voltage ($V_{c,o}$), $v_{c,noise}$ is transferred to port 2, resulting in additional noise at the output port (see Fig. 3(a)). Additionally, clock-edge fluctuations during the discharging phase also lead to uncertainty in the amount of charge discharged to port 2, leading to an additional noise that is proportional to the strength of the input signal and clock jitter during the discharging phase. We rigorously analyze this phenomenon in [51] by modeling the clock timing jitter at the rising and falling edges with Gaussian random variables δt_r and δt_f, with a zero mean and a variance of $\delta t_{r,rms}$ and $\delta t_{f,rms}$ respectively.

In switched capacitor circuits, a sinusoidal modulation clock signal is converted to a square wave clock signal through a low-noise voltage-limiting buffer. Multiple phases of the square-wave clock signal to drive the different layers and ports are then generated using multi-phase clock-generation circuitry. The phase noise in the sinusoidal input and from the voltage limiter will result in a correlated phase noise across all the non-overlapping phases. On the other hand, the phase noise contributed by the multi-phase clock-generation circuitry can lead to an uncorrelated noise across the non-overlapping phases. We have shown that for the uncorrelated clock phase noise, which is what we observe in our prototype, for a sinusoidal input at port 1, the output noise power spectral density (PSD) at port 2 due to the clock jitter (i.e., noise power at port 2 within a bandwidth of 1Hz) can be expressed as a function of the input power, input frequency and clock jitter as

$$N(\omega_o) = P_1 \frac{T_S}{N}\left(S_{21}(\omega_{in}) \times \frac{F_l(\omega_o)}{F_l(\omega_{in})}\right)^2 \begin{bmatrix} \{|K_1(\omega_{in})^2|+|K_2(\omega_o)^2|\}\delta t_{r,rms}^2 \\ +\{|K_2(\omega_{in})^2| + |K_1(\omega_o)^2|\}\delta t_{f,rms}^2 \end{bmatrix}, \qquad (2)$$

where $P_1 = \frac{A_1^2}{4Z_o}$ and ω_{in} represents the input power and input frequency at port 1, $S_{21}(\omega_{in})$ represents the transmission from port 1 to port 2 as expressed in (1), and $F_l(\omega), K_1(\omega)$, and $K_2(\omega)$ are

$$Y(\omega) = \frac{T_s}{N}\left(\frac{1}{\tau} + j\omega\right), F_l(\omega) = \frac{1 - \exp\left(-Y(\omega)\right)}{Y(\omega)},$$

$$K_1(\omega) = -\frac{N}{T_S}\frac{Y(\omega)\exp\left(-Y(\omega)\right)}{1 - \exp\left(-Y(\omega)\right)}, K_2(\omega) = -\frac{1}{\tau} + \frac{N}{T_s}\frac{Y(\omega)}{1 - \exp\left(-Y(\omega)\right)}. \quad (3)$$

See [51] for detailed derivation. From (2), it can be seen that the PSD of the output noise is proportional to the input power and the variance of the clock jitter. This clock-induced noise will be an additive noise, in addition to the thermal noise present at port 2. The effect of the noise added by a device is typically characterized using noise figure (*NF*), which captures the degradation in the signal-to-noise ratio (*SNR*) produced by the device (i.e., $NF = SNR_{in}/SNR_{out}$). The NF from port 1 to port 2 at a frequency ω_o in presence of a strong input signal at port can be calculated as

$$NF_{21}(\omega_o) = \frac{SNR_{in}}{SNR_{out}} = S_{21}(\omega_o) \times \left(1 + \frac{N(\omega_o)}{kT}\right), \quad (4)$$

where $S_{21}(\omega_o)$ is the transmission from port 1 to port 2 (see eq. (1)), $N(\omega_o)$ represents the output noise due to the interaction between the clock jitter and input signal (see (2)), k represents the Boltzmann constant, and T is the absolute temperature. In this noise analysis, the small matching inductors are ignored. Even in the presence of matching inductors, the operation principle of the circulator remains unchanged (except for a current boosting in the charging and discharging profiles), and therefore the clock-induced noise phenomenon will still be observed.

Fig. 3(b) shows the simulated port 1 to port 2 noise figure of our 65nm CMOS 8-path, 3-port, helicoidally rotating circulator across varying incident power at port 1 ($f_{in} = f_s = 500MHz$ and $f_o = 2f_s = 1GHz$). Note that our 65nm CMOS multi-phase clock generating circuit (discussed in the implementation section) generates multi-phase clock pulses with mostly-uncorrelated phase noise with a variance of $\delta t_{r,rms}$= 40 fs and $\delta t_{f,rms}$= 32 fs for the rising and falling edges respectively. Figure 3(c) shows the port 1 to port 2 noise figure across various input powers and input frequencies at port 1. The simulated noise figures are obtained using the Cadence Spectre RF (PSS solver) [62]. As expected, the noise figure degradation increases with the input power. Additionally, the noise figure degradation also becomes higher when driven with higher frequency input. As can be seen, our analysis closely predicts the simulated noise figure for uncorrelated clock phase noise across the clock phases.

On the other hand, when the clock jitter is correlated across the multi-phase clock pulses, it has minimal impact to the output noise of the helicoidal circulator across the frequency range of $|f_o - f_{in}| \ll Nf_s$, where f_{in} is the input frequency and f_o is the frequency at which output noise is measured. Fig. 3(d) depicts the theoretically calculated noise figure across various TX powers for various input frequencies, when driven with correlated multi-phase clocks. For the specific case of N=8 and $f_s = 500MHz$, the correlated clock jitter has no impact across ~800MHz around the input frequency. Therefore, techniques that ensure noise correlation across the multi-phase pulses, such as the retiming of the clocks with the input square-wave clock toward the end of the inverter chain [63], are expected to eliminate this effect of dynamic clock noise appearing at the output without a significant impact on clock path power consumption. These insights were not available to us at the time of design of this prototype, and so the clock path implemented is dominated by un-correlated noise.

IV. Implementation and Experimental Verification of a 3-Port Chip-Scale Circulator

As a proof of concept, we implemented a 3-port integrated circulator in a 65nm CMOS chip modulated at 500MHz and operating over DC-1GHz. Fig. 4a shows the circuit diagram and the chip microphotograph. The circulator consists of 8 parallel non-overlapping layers, each consisting of a 2.5pF capacitor connected to 3-ports through three 51μm/60nm transistor switches with an ON resistance of 6Ω. The modulation path consists of pseudo-differential buffers to generate square-waves from the input 2GHz differential sinusoidal modulation input. These square wave signals were divided by a factor of 4 and then fed to a non-overlapping clock-generator to generate the 8 phases of 500MHz, 12.5% duty cycle non-overlapping clocks required by the commutated switches. We leveraged the inductance from bond wires between the CMOS chip and the QFN package as the 3nH inductor required for improved matching, resulting in an extremely compact area of 0.19mm^2 and a miniaturization factor of 2×10^6 (defined as $\lambda^2_{\text{center}}$/area, where λ_{center} is the free space wavelength at the center frequency). This miniaturization factor is 10^2-$10^4\times$ larger than prior approaches (Fig. 4b). Fig. 4c summarizes the performance comparison of the proposed work with prior integrated circulators.

Figure 5 summarizes the measured performance of our prototype with symmetric performance across the 3 ports. For a modulation frequency f_S=500MHz, the clocking circuitry consumes 20mW and the circulator exhibits transmission losses ranging from 3.1dB - 4.3dB (Fig. 5a), isolation > 18dB (Fig. 5b) and matching< -15dB (Fig. 5c) across a frequency range of DC - 1GHz. The measured noise figure ranges from 3dB – 4dB (Fig. 5d) and is consistent with the insertion loss, indicating no degradation in the noise performance due to modulation clock noise. The power handling of a switching device is limited by the LO swing that drives the gate of the transistor switches. Using conventional digital drivers withs supply voltage of 1.2V, the LO swing

in this implementation is from 0V to 1.2V, which lead to the transmission path to compress by 1dB at an excitation power of +1.5dBm. Employing LO boosting schemes presented in [64] to enhance the power handling will be an interesting research direction. The measured input-referred third-order intercept point (IIP3) for the transmission and isolation paths are +20dBm and >+25dBm respectively. These linearity metrics remain quite constant across the bandwidth of operation as shown in Fig. 5e. The isolation remains constant across an excitation power range of -15dBm to +5dBm (Fig. 5f). It is desired that the circuit performance of these multiport non-reciprocal devices remains unchanged when multiple ports are excited simultaneously. To this end, we measured the compression of the transmission path from port 2 to port 3 under application of a large signal at port 1- with a power of +6.2dBm at port 1, 2-to-3 transmission compresses by 1dB.

In communication systems, circulators are commonly used for achieving simultaneous-transmit-and-receive operation. For instance, ports 1-3 can be connected to the transmitter (TX), antenna (ANT), and receiver (RX) respectively. The presence of strong signal at port 1 (TX) can desensitize the port2 to port 3 path due to the interaction between TX signal and the clock noise. This is identical to the mechanism described in Section IV, with the exception that we now examine the noise added to port 2-to-3 transmission due to a powerful signal at port 1, as opposed to the noise added to port 1-to-2 transmission as considered in Section IV. We measured the ANT-RX noise figure as a function of TX power using the gain method by observing the rise in the noise floor at the RX port using the measurement setup shown in Fig. 6(a). A strong TX tone is incident at 1.01 GHz, and the rise in the noise floor at a slight offset frequency of 975 MHz is monitored. The surface acoustic wave (SAW) filter at 975 MHz allows monitoring the noise floor at that frequency while attenuating the residual TX leakage at 1.01 GHz and preventing it from saturating

the pre-amplifier and the spectrum analyzer. An isolator is used ahead of the SAW filter to ensure a matched termination for the circulator outside the SAW bandwidth. Fig. 6 (b) shows the measured ANT-RX noise figure across varying TX power. At a power level equal to the 1dB compression point of the TX-ANT, the NF degrades by ≈2.8 dB with a measurement accuracy of ±1 dB. Our post layout simulations suggest that at a TX power level of TX-ANT P1 dB, the NF degradation is ≈2 dB, confirming the reciprocal mixing phenomenon described in the previous section, and expected in these parametric systems. Improving the signal-induced NF with the design of a clock path design with correlated clock pulses, as suggested by our analysis in the previous section, is an interesting research direction.

V. Discussion

Our experiments show that synthetic helicoidal motion of an electrostatic medium opens a new paradigm for magnet-free non-reciprocity, enabling unprecedented wideband non-reciprocity, extending from DC to a frequency only limited by technological constraints, while at the same time miniaturizing the device to infinitesimal form factors. Fig. 3b compares the implemented 65nm CMOS prototype to prior time-modulated circulator demonstrations in terms of fractional bandwidth (defined as -3dB transmission bandwidth divided by the center frequency) versus miniaturization factor. This quasi-electrostatic circulator offers the highest fractional bandwidth along with a huge miniaturization factor which is 10^2-10^4× larger than prior approaches.

Within the measured insertion loss of 3.1 – 4.3dB, harmonic conversion due to usage of only 8 layers contributes up to 1-1.7dB, switch ON-resistance contributes 1dB, switch parasitic capacitances contribute 0.6-0.8dB, clocking imperfections contribute 0.3dB and the rest is associated with other non-idealities such as resistive loss of the matching bond-wire inductor and

package parasitics. The implementation based purely on switches and capacitors benefits from the scaling of semiconductor technology. For instance, a 4-layer, 3-port circulator, with $Nf_s = 4\text{GHz}$ implemented in a 22nm CMOS process can achieve insertion losses of 1.6-2.2dB across DC-1GHz and is ultimately limited by harmonic conversion. A quantification of the losses due to harmonic conversion can be found in [51]. Matching networks that reduce the losses associated with harmonic conversion represent an interesting future research direction. We have also analyzed the impact of modulation signal noise on the noise performance of time-modulated structures and presented methods for mitigating this effect. We corroborated our theoretical findings with simulation and measurement results.

The concepts developed in this work are applicable to non-reciprocal components used in various applications. Wireless communication devices today operate across multiple frequency bands and standards, and such a wideband circulator eliminates the need for multiplexing of multiple narrowband bulky and expensive magnetic circulators. In software-defined spectrum sharing scenarios the secondary users continuously monitor the spectrum for the presence of primary user, and such wideband circulator can enhance the receiver sensitivity by suppressing the TX-interference [65]. This device can also be deployed into wideband simultaneous-transmit-and-receive radars such as ground-penetrating radars that operate from DC – to GHz frequencies [66]. Such a compact, reconfigurable, ultra-wideband circulator can also serve as an ideal building block to realize Floquet topological meta-insulators [47] on a chip-scale with an ultra-wideband topologically-protected bandgap that can potentially revolutionize our ability to control and route electromagnetic waves in multiple-input and multiple-output (MIMO) systems.

Data Availability

The authors declare that all relevant data are included in the paper and in [51]. Additional data are available from the corresponding authors upon request.

Acknowledgments

This work was supported by the DARPA SPAR program and the Air Force Office of Scientific Research MURI program.

References

[1] Nagulu, A., Reiskarimian, N., Chen, T., Garikapati, S., Kadota, I., Dinc, T., Garimella, S. L., Kohli, M., Levin, A. S., Zussman, G. & Krishnaswamy, H. Doubling Down on Wireless Capacity: A Review of Integrated Circuits, Systems, and Networks for Full Duplex. *Proc. IEEE* **112**, 405-432 (2024).

[2] Tanaka, S., Shimimura, N. & Ohtake, K. Active circulators–The realization of circulators using transistors. *Proc. IEEE* **53**, 260–267 (1965).

[3] H.-S. Wu, C.-W. Wang, and C.-K. C. Tzuang. CMOS Active Quasi-Circulator With Dual Transmission Gains Incorporating Feedforward Technique at K-Band. *IEEE Transactions on Microw. Theory Techn.*, vol. **58**, 2084–2091 (2010).

[4] Chang, J. F., Kao, J. C., Lin, Y. H. & Wang, H . Design and Analysis of 24-GHz Active Isolator and Quasi-Circulator. *IEEE Transactions on Microw. Theory Techn.* **63**, 2638–2649 (2015).

[5] Kodera, T., Sounas, D. L. & Caloz, C. Artificial Faraday rotation using a ring metamaterial structure without static magnetic field. *Appl. Phys. Lett.* **99**, 031114 (2011).

[6] Carchon, G. & Nanwelaers, B. Power and noise limitations of active circulators. *IEEE Trans. Microw. Theory Techn.* **48**, 316–319 (2000).

[7] Fan, L. , Wang, J., Varghese, L. T., Shen, H., Niu, B., Xuan, Y. Weiner, A. M. & Qi, M. An all-silicon passive optical diode. *Science* **335**, 447–450 (2012).

[8] Gallo, K., Assanto, G., Parameswaran, K. R. & Fejer, M. M. All-optical diode in a periodically poled lithium niobate waveguide. *Appl. Phys. Lett.* **79**, 314–316 (2001).

[9] Mahmoud, A. M., Davoyan, A. R. & Engheta, N. All-passive nonreciprocal metastructure. *Nat. Commun.* **6**, 8359 (2015).

[10] Sounas, D.L., Soric, J. & Alù, A. Broadband Passive Isolators Based on Coupled Nonlinear Resonances. *Nat. Electron.* **1**, 113-119 (2018).

[11] Yang, K. Y., Skarda, J., Cotrufo, M., Dutt, A., Ahn, G. H., Sawaby, M., Vercuysse, D., Arbabian, A., Fan, S., Alù, A., Vuckovic, J. Inverse-Designed Non-Reciprocal Pulse Router for Chip-Based LiDAR. *Nat. Photon.* **14**, 369-374 (2020).

[12] Cotrufo, M., Mann, S. A., Moussa, H., & Alù, A. Nonlinearity-Induced Nonreciprocity – Part I. *IEEE Trans. Microw. Theory Techn.* **69**, 3569-3583 (2021), (***invited paper***).

[13] Cotrufo, M., Mann, S. A., Moussa, H., & Alù, A. Nonlinearity-Induced Nonreciprocity – Part II. *IEEE Trans. Microw. Theory Techn.* **69**, (2021), 3584-3597 (***invited paper***).

[14] Sounas, D.L. & Alù, A. Non-reciprocal photonics based on time modulation. *Nat. Photon.* **11,** 774–783 (2017).

[15] Ranzani, L. & Aumentado, J. Circulators at the Quantum Limit: Recent Realizations of Quantum-Limited Superconducting Circulators and Related Approaches. *IEEE Microw. Mag.* **20**, 112-122 (2019).

[16] Nassar, H., Yousefzadeh, B., Fleury, R., Ruzzene, M., Alù, A, Daraio, C., Norries, A. N., Huang, G. & Haberman, M. R. Nonreciprocity in acoustic and elastic materials. *Nat Rev. Mater.* **6**, 667-685 (2020).

[17] Nagulu, A., Reiskarimian, N. & Krishnaswamy, H. Non-reciprocal electronics based on temporal modulation. *Nat. Electron.* **3,** 241–250 (2020).

[18] Williamson, I.A., Minkov, M., Dutt, A., Wang, J., Song, A. Y. & Fan, S. Integrated Nonreciprocal Photonic Devices With Dynamic Modulation. *Proc. of IEEE* **108**, 1759-1784 (2020).

[19] Kord, A., Sounas, D. & Alù, A. Microwave Nonreciprocity. *Proc. of IEEE* **108**, 1728-1758 (2020), (***invited paper***).

[20] Fleury, R., Sounas, D. L., Sieck, C. F., Haberman, M. R. & Alù, A. Sound isolation and giant linear nonreciprocity in a compact acoustic circulator. *Science* **343**, 516–519 (2014).

[21] Sounas, D. L. & Alù, A. Angular-momentum-biased nanorings to realize magnetic-free integrated optical isolation. *ACS Photon.* **1**, 198–204 (2014).

[22] Estep, N. A., Sounas, D. L., Soric, J. & Alu, A. Magnetic-free nonreciprocity and isolation based on parametrically modulated coupled-resonator loops. *Nat. Phys.* **10**, 923–927 (2014).

[23] Yang, C. & Gui, P. 85-110GHz CMOS Magnetic-Free Nonreciprocal Components For Full-Duplex Transceivers. *IEEE J. Solid-State Circuits* **54**, 368-379 (2019).

[24] Kord, A., Tymchenko, M., Sounas, D. L., Krishnaswamy, H. & Alù, A. CMOS Integrated Magnetless Circulators Based on Spatiotemporal Modulation Angular-Momentum Biasing. *IEEE Trans. Microw. Theory Techn.* **67**, 2649–2662 (2019).

[25] Torunbalci, M. M., Odelberg, T. J., Sridaran, S., Ruby, R. C. & Bhave, S. A. An FBAR circulator. *IEEE Microw. Compon. Lett.* **28**, 395–397 (2018).

[26] Yu, Y., Michetti, G., Kord, A., Sounas, D., Pop, F. V., Kulik, P., Pirro, M., Qian, Z., Alu, A. & Rinaldi, M. Magnetic-free radio frequency circulator based on spatiotemporal commutation of MEMS resonators. *Proc. IEEE Micro Electro Mech. Syst. (MEMS)*, 154–157 (2018).

[27] Xu, C. & Piazza, G. Magnet-less circulator using AlN mems filters and CMOS RF switches. *J. of Microelectromechanical Syst.* **28**,409-418 (2019).

[28] Reiskarimian, N. & Krishnaswamy, H. Magnetic-free nonreciprocity based on staggered commutation. *Nat. Commun.* **7**, 11217 (2016).

[29] Dinc, T., Tymchenko, M., Nagulu, A., Sounas, D., Alu, A. & Krishnaswamy, H. Synchronized conductivity modulation to realize broadband lossless magnetic-free nonreciprocity. *Nat. Commun.* **8**, 795 (2017).

[30] Biedka, M. M., Zhu, R., Xu, Q. M. & Wang, Y. E. Ultra-wide band non-reciprocity through sequentially-switched delay lines. *Sci. Rep.* **7**, 40014 (2017).

[31] Biedka, M., Rodgers, P., Gutierrez, N., LaRocca, T. & Wang, Y. E. 100MHz to 1GHz On-Chip Circulator with Integrated Driver Amplifiers. *IEEE International Mcrow. Symp.*, 1488–1491 (2019).

[32] Lu, R., Krol, J., Gao, L. & Gong, S. A Frequency Independent Framework for Synthesis of Programmable Non-reciprocal Networks. *Sci. Rep.* **8,** 14655 (2018).

[33] Bahamonde, J., Kymissis, I., Alù, A. & Krishnaswamy, H. 1.95-GHz circulator based on a time-modulated electro-acoustic gyrator. *Proc. IEEE Int. Symp. Antennas and Propagation and USNC-URSI Radio*, (2018).

[34] Lu, R., Manzaneque, T., Yang, Y., Gao, L., Gao, A. & Gong, S. A Radio Frequency Non-reciprocal Network Based on Switched Acoustic Delay Lines. *IEEE Trans. Microw. Theory Techn.* **67**, 1516-1530 (2019).

[35] Lira, H., Yu, Z., Fan, S. & Lipson, M. Electrically driven nonreciprocity induced by interband photonic transition on a silicon chip. *Phys. Rev. Lett.* **109**, 033901 (2012).

[36] Kang, M., Butsch, A. & Russell, P. S. J. Reconfigurable light-driven opto-acoustic isolators in photonic crystal fibre. *Nat. Photonics* **5**, 549–553 (2011).

[37] Yu, Z. & Fan, S. Complete optical isolation created by indirect interband photonic transitions. *Nat. Photonics* **3**, 91–94 (2008).

[38] Shi, Y., Han, S. & Fan, S. Optical circulation and isolation based on indirect photonic transitions of guided resonance modes. *ACS Photonics* **4**, 1639 (2017).

[39] Qin, S., Xu, Q. & Wang, Y. E. Nonreciprocal components with distributedly modulated capacitors. *IEEE Trans. Microw. Theory Techn.* **62**, 2260–2272 (2014).

[40] Taravati, S. Self-biased broadband magnet-free linear isolator based on one-way space-time coherency, *Phys. Rev. B* **96**, 235150 (2017).

[41] Taravati, S., Chamanara, N. & C. Caloz, Nonreciprocal electromagnetic scattering from a periodically space-time modulated slab and application to a quasisonic isolator, *Phys. Rev. B* **96**, 165144 (2017).

[42] Taravati, S. & Eleftheriades, G. V. Full-Duplex Nonreciprocal Beam Steering by Time-Modulated Phase-Gradient Metasurfaces, *Phys. Rev. Applied* **14**, 014027 (2020).

[43] Taravati, S. & Caloz, C. Mixer-duplexer-antenna leaky-wave system based on periodic space-time modulation, *IEEE Trans. Antennas Propagat.* **65**, 442 (2017).

[44] Shaltout, A., Kildishev, A. & Shalaev, V. Time-varying metasurfaces and Lorentz nonreciprocity, *Opt. Mat. Exp.* **5**, 2459 (2015).

[45] Shi, Y. & Fan, S. Dynamic non-reciprocal meta-surfaces with arbitrary phase reconfigurability based on photonic transition in meta-atoms, *Appl. Phys. Lett.* **108**, 021110 (2016).

[46] Fleury, R., Khanikaev, A. B. & Alu, A. Floquet topological insulators for sound. *Nat. Commun.* **7**, 11744 (2016).

[47] Nagulu, A., Ni, X., Kord, A., Tymchenko, M., Garikapati, S., Alù, A. & Krishnaswamy, H. Chip-scale Floquet topological insulators for 5G wireless systems. *Nat. Electron.* **5**, 300–309 (2022).

[48] Franks, L.E. & Sandberg, I.W. An alternative approach to the realization of network transfer functions: the N-path filter. *Bell System Technical Journal* **39**, 321-1350 (1960).

[49] Ghaffari, A., Klumperink, E. A. M., Soer, M. C. M. & Nauta, B. Tunable High-Q N-Path Band-Pass Filters: Modeling and Verification. *IEEE J. Solid-State Circuits* **46**, 998-1010 (2011).

[50] Tymchenko, M., Sounas, D., Nagulu, A., Krishnaswamy, H. & Alù, A. Quasielectrostatic wave propagation beyond the delay-bandwidth limit in switched networks. *Physical Review X* **9**, 031015 (2019).

[51] See Supplemental Material at [URL will be inserted by publisher] for detailed analytical derivations and further discussion on the impact of noise.

[52] Lathi, B.P., Modern Digital and Analog Communication Systems 3e Osece. *Oxford University Press Inc.* (1998).

[53] Nagulu, A., Dinc, T., Xiao, Z., Tymchenko, M., Sounas, D.L., Alù, A. & Krishnaswamy, H. Nonreciprocal components based on switched transmission lines. *IEEE Trans. Microw. Theory Techn.* ***66***, 4706-4725 (2018).

[54] Doerr, C. R., Dupuis, N. & Zhang, L. Optical isolator using two tandem phase modulators. *Optics Letters* **36**, 4293 (2011).

[55] Lin, Q., Wang, J. & Fan, S. Compact dynamic optical isolator based on tandem phase modulators. *Optics Letters* **44**, 2240 (2019).

[56] Reiskarimian, N., Zhou, J., Chuang, T. & Krishnaswamy, H. Analysis and Design of Two-Port N-Path Bandpass Filters With Embedded Phase Shifting. *IEEE Trans. Circuits Syst. II: Express Briefs* **63**, 728-732 (2016).

[57] Ernst, C., Postoyalko, V. & Khan, N.G. Relationship between group delay and stored energy in microwave filters. *IEEE Trans. Microw. Theory Techn.* **49**, 192-196 (2001).

[58] Mann, S.A., Sounas, D.L. & Alù, A., Nonreciprocal cavities and the time–bandwidth limit. *Optica*, **6**,104-110 (2019).

[59] see ADS at https://www.keysight.com/

[60] Dinc, T., Nagulu, A. & Krishnaswamy, H. A Millimeter-Wave Non-Magnetic Passive SOI CMOS Circulator Based on Spatio-Temporal Conductivity Modulation. *IEEE J. Solid-State Circuits* **52**, 3276-3292 (2017).

[61] Xiao, Z.*, Sounas, D. L.*, Nagulu, A. *, Tymchenko, M., Krishnaswamy, H. & Alù, A. Role of synchronization in magnetless nonreciprocal devices based on commutated transmission lines. *Phys. Rev. Applied* **13**, 064033 (2020). (* equal contribution).

[62] see Cadence Spectre Solver at https://www.cadence.com/en_US/home.html

[63] Andrews, C. & Molnar, A. C. A passive mixer-first receiver with digitally controlled and widely tunable RF interface. *IEEE J. Solid-State Circuits* **45**, 2696–2708 (2010).

[64] Nagulu, A., Chen, T., Zussman, G. & Krishnaswamy, H. Multi-Watt, 1GHz CMOS Circulator Based on Switched-Capacitor Clock Boosting. *IEEE J. Solid-State Circuits* **55**, 3308-3321 (2020).

[65] Parvini, M., Zarif, A. H., Nouruzi, A., Mokari, N., Javan, M. R., Abbasi, B., Ghasemi, A. & Yanikomeroglu, H. Spectrum Sharing Schemes From 4G to 5G and Beyond: Protocol Flow, Regulation, Ecosystem, Economic. *IEEE Open J. Commun. Society* **4**, 464-517, (2023).

[66] Huang, R., Zhang, Y., Decrossas, E., Seshadri, A., Liang, C. J., Chang, M. C. F. & Tang, A. A 0.1–4.0-GHz Inductorless Direct-Sequence Spread-Spectrum-Based Ground-Penetrating Radar System-on-Chip. *IEEE Microw. Wireless Components Letters* **31**, 827-830 (2021).

Figures

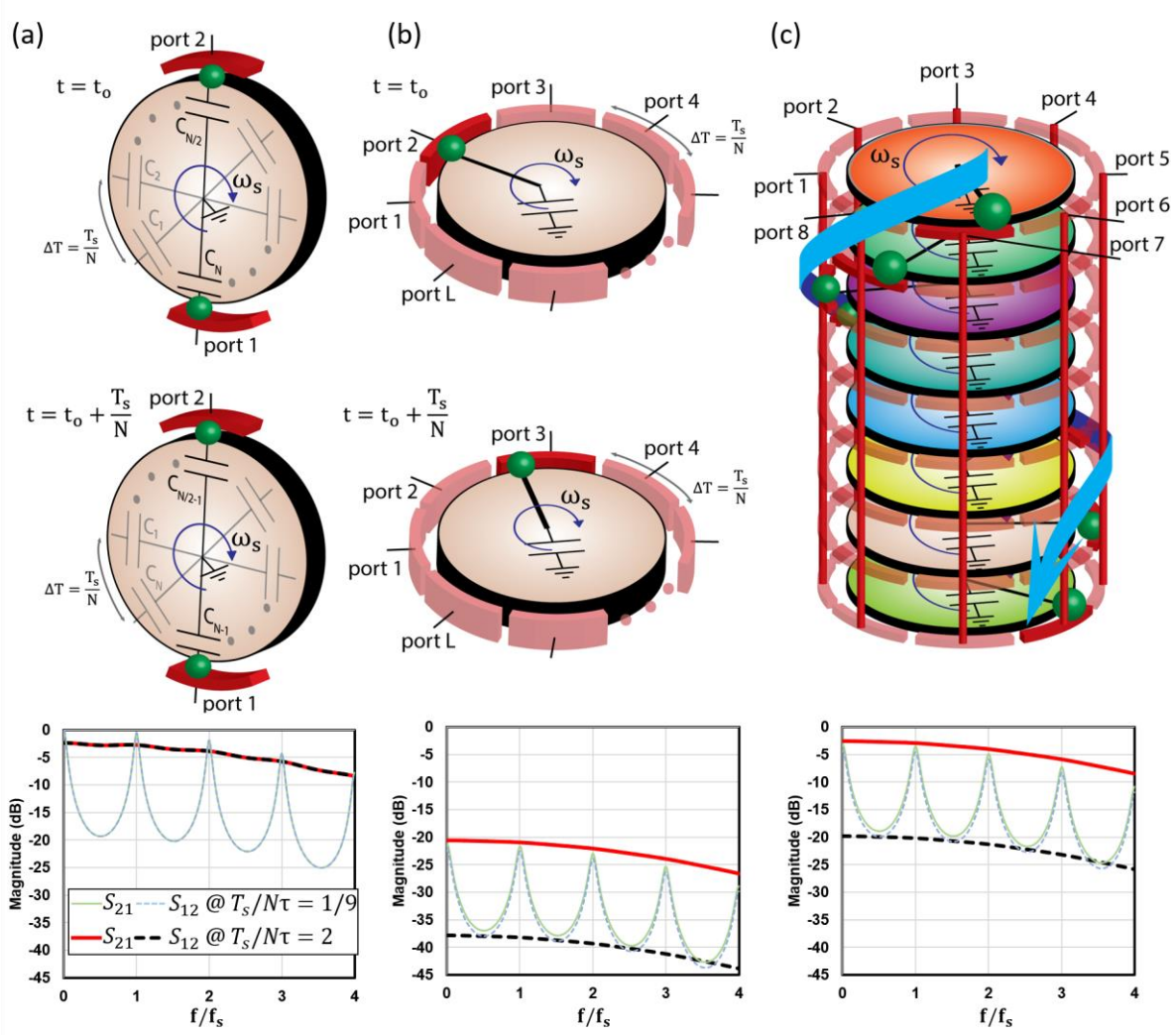


Figure 1. Ultra-broadband electrostatic circulator with synthetic helicoidal rotation enabled by vertical-plane rotation and horizontal-plane rotation of an electrostatic ring resonator. (a) Schematic of the 2-port, N-path structure enabling electrostatic propagation between port 1 and port 2. The *N* capacitors are vertically rotating at rate ω_s and connect to each port (red frame) for a period $\frac{T_s}{N}$. The top panel is the N-path configuration at time t_0 and the middle panel is the configuration at a subsequent time $t_0 + \frac{T_s}{N}$. The bottom panel contains the magnitude of the scattering parameters for the 2-port, N-path structure in Fig. 1a, for two different ratios $\frac{T_s}{N\tau} = \frac{1}{9}$ (filtering) and 2 (slow-wave delay). (b) Schematic of the electrostatic ring with horizontal-plane rotation of the switch at rate ω_s with L ports. The l^{th} port is located at angular phase $\phi = l\frac{360^\circ}{N}$.

Each port is connected for a period of $\frac{T_s}{N}$ to the capacitor. The top panel shows the switch configuration at time t_0, and the middle panel at time $t = t_0 + \frac{T_s}{N}$. The magnitude of the scattering parameters for the electrostatic ring resonator with 3 ports for two different ratios $\frac{T_s}{N\tau} = \frac{1}{9}$ and 2 are shown in the bottom panel. (c) A combination of the electrostatic ring in Fig. 1b and the N-path structure in Fig. 1a forms a helicoidal shape for the switch locus at any given time t_0. The magnitude of the scattering parameters for the electrostatic circulator with 8 parallel electrostatic ring resonators and 3 ports is shown in the bottom panel, verifying ultra-broadband non-reciprocal circulation for $\frac{T_s}{N\tau} = \frac{1}{9}$. The results in (a)-(c) are for $N = 8$, $Z_0 = 50\ \Omega$ and $T_s = \frac{1}{f_s} = 2$ ns.

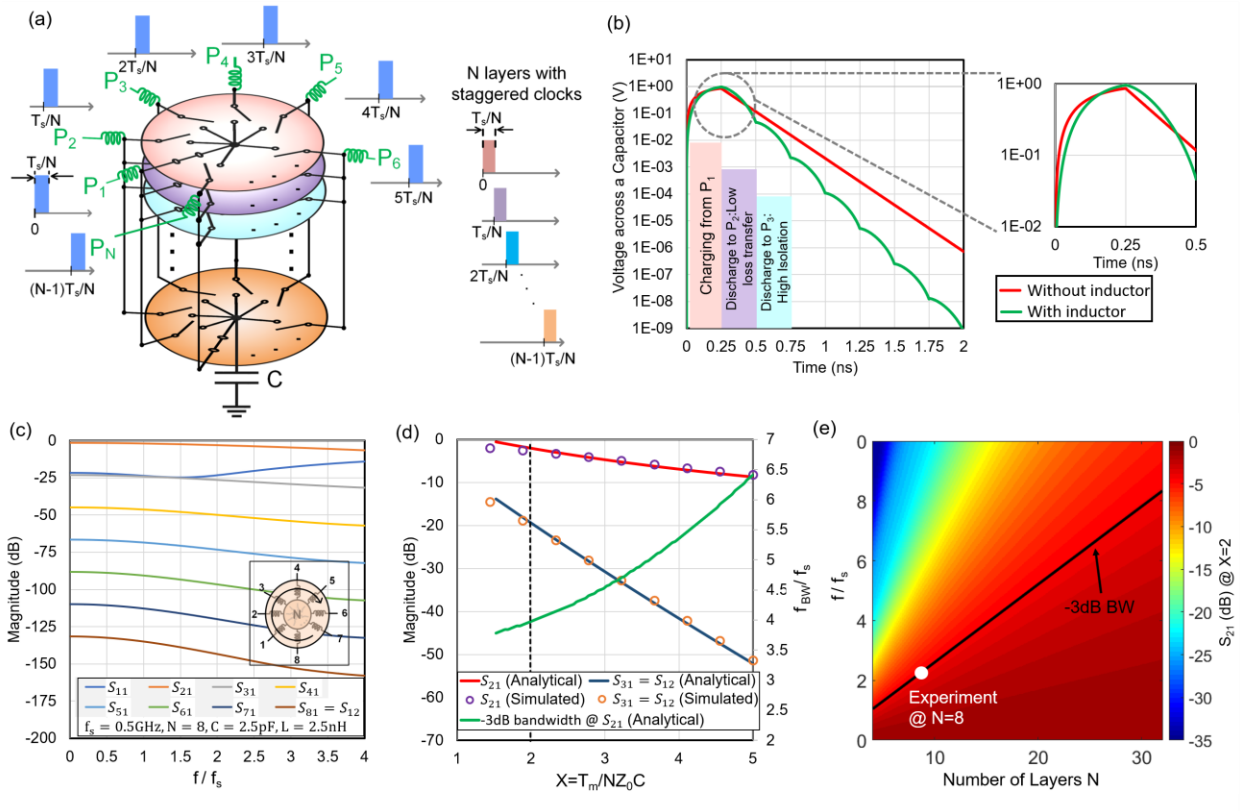


Figure 2. (a) Circuit diagram of the N-port, ultra-broadband quasi-electrostatic circulator realized using a helicoidally-rotating electrostatic ring along with small inductors at the ports to enhance the matching, loss and isolation. (b) Evolution of the voltage on one of the shunt capacitors across time for an excitation at port 1 with and without the small matching inductors of 3nH at the ports. (c) Magnitude of the scattering parameters of an 8-port circulator with Z_0 =50Ω, N=8, C = 2.5 pF, f_s = 0.5 GHz, L=2.5nH at all the ports. (d) Scattering parameters $|S_{21}(f_s)|$ and $|S_{31}(f_s)|$ in dB scale and -3dB bandwidth of $|S_{21}(f)|$ for varying ratio $x = \frac{T_s}{N\tau}$ with $N = 8$ without the matching inductors at the ports. The solid lines indicate the results from analytical formulas, while the circles indicate simulation results. The dashed line indicates the ratio used in the experiment. (e) 2D plot of the analytically calculated scattering parameters (without matching inductors) as a function of the normalized frequency f/f_s and the number of layers N for $x = 2$. The white circle in (e) indicates the ratio used in the experiment and the black solid line indicates the contour of the -3dB bandwidth frequencies.

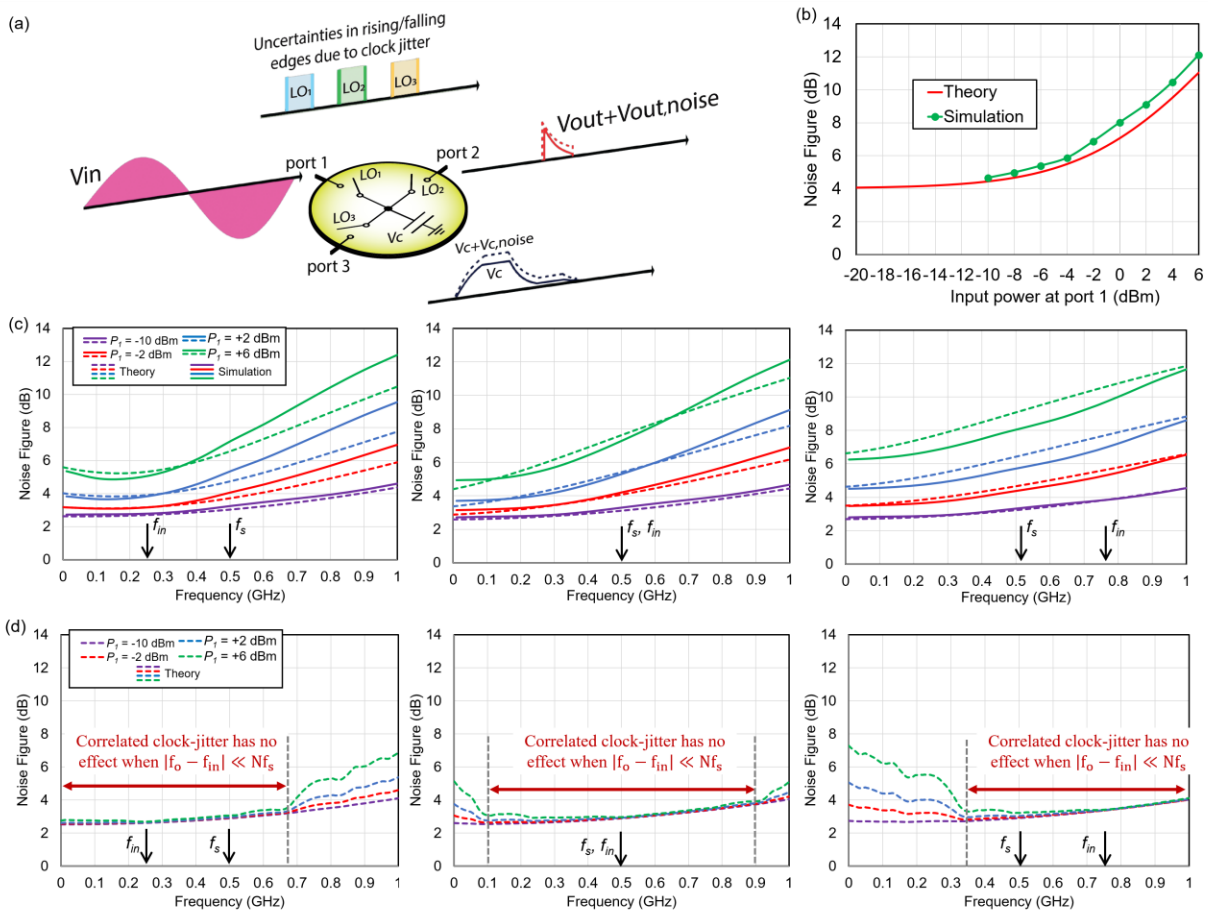
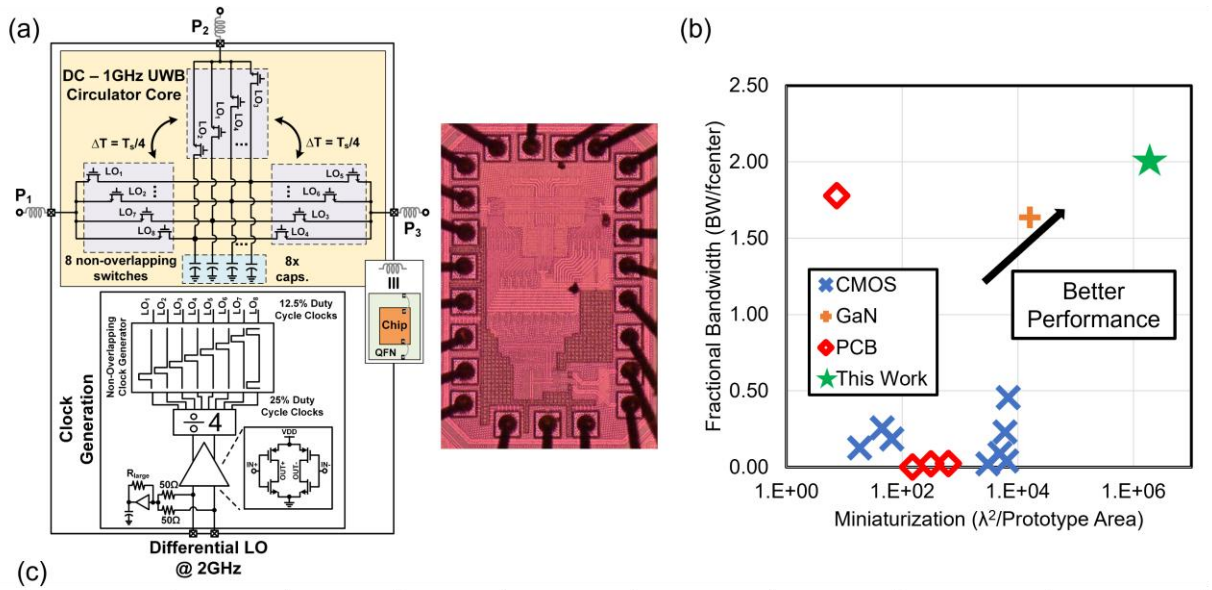


Figure 3. (a) Dynamic noise mechanism generating input and clock-jitter dependent output noise. Port 1 to port 2 noise figure of our 65nm CMOS 8-path, 3-port, helicoidally rotating circulator as a function the input power at port 1: (b) Theoretically-calculated and simulated noise figure across input power incident at port 1 ($f_{in} = f_s = 500MHz$ and $f_o = 2f_s = 1GHz$). (c) Noise figure across various TX powers for input frequencies of f_{in} = 250MHz, 500MHz and 750MHz respectively, when driven with the same clocks as panel (b). (d) Theoretically-calculated noise figure across various TX powers for input frequencies of f_{in} = 250MHz, 500MHz and 750MHz respectively, when driven with multi-phase clocks with correlated noise.



(c)

	TMTT 2010 [3]	TMTT 2015 [4]	TMTT 2019 [24]	Nat. Com. 2016 [28]	Nat. Com. 2017 [29]	JSSC 2020 [63]	IMS 2019 [31]	This work
Technique	Active Circulator	Active Circulator	STM-AM	N-path-filter circulator	Spatio-Temporal Conductivity Mod. across Delay Line	Switched T-Line based Circulator	Sequentially Switched Delay Lines	**UWB Circulator based on Commutated Switched Capacitor Networks**
Technology	180nm CMOS	180nm CMOS	180nm CMOS	65nm CMOS	45nm CMOS SOI	180nm CMOS	0.2μm GaN	**65nm CMOS**
Center Frequency	23.75 GHz	24 GHz	0.91 GHz	0.61-0.975 GHz	25 GHz	0.95 GHz	0.55 GHz	**0.5GHz**
Transmission BW	1.5 GHz	0.38 GHz	0.02 GHz	0.03 GHz	4.6 GHz	0.17 GHz	0.9 GHz	**DC – 1GHz**
Modulation Freq.	N/A	N/A	0.1 GHz	1GHz	8.3GHz	0.2 GHz	1.25 GHz	**500MHz**
Off-Chip Components	No	No	Yes	Yes	No	No	No	**No**
Supply Voltage	1.8 V	1.2 V	3.3 V	1.2 V	1.2 V	2 V	12V	**1.3V**
TX-ANT/ANT-RX Transmission	+22.4 dB / +12.3dB	-5.7 dB / -5.7 dB [1]	-4.8 dB/-4.8 dB [1]	-1.7 dB / -1.7 dB [1]	-3.3 dB / -3.2 dB [1]	-2.1 dB / -2.1dB [1]	-3dB to -4.1dB/ -3dB to -4.1dB [2]	**-3.1 dB to -4.3dB/ -3.1 dB to -4.3dB [2]**
TX-RX Isolation BW (BW/f_{center})	1% (>15dB)	1.6% (>20dB)	2.4% (>20dB)	1.9%(>25dB)	>18.5 dB (18%) [3]	18% (>25dB)	163% (>18dB) [5]	**200% (>18dB)**
ANT-RX NF	17 dB	8 dB – 10 dB	5.2 dB	4.3 dB	3.3 dB - 4.4 dB	2.5 dB	N/R	**3.1dB – 4.1dB**
TX-ANT/ANT-RX IP_{1dBS}	-19.18 dBm	+9.5 dBm / N/R	+6.1dBm / +6dBm	+27.5dBm/ N/R	>+21.5 dBm/ >+21dBm	>+34 dBm / 17dBm	17dBm / 17dBm	**+1.4dBm/+1.4dBm**
TX-ANT/ANT-RX IIP3s	-11 dBm	N/R	N/R / N/R	+8.7dBm/ N/R	20.1 dBm / 19.9 dBm	+50dBm/+36.3dBm	N/R / N/R	**+20 dBm / +20 dBm**
TX-RX Compression (20dB / 15dB Levels)	N/R	N/R	N/R	N/R	N/A / +21 dBm	>+34dBm / >+34dBm	N/R	**>+5dBm / >+5dBm**
TX-induced ANT-RX P_{1dB} Compression	N/R	N/R	N/R	N/R	N/R	>+29.3 dBm	N/R	**+6.2dBm**
PDC	144.8 mW	7.2 mW	64mW	59 mW	78.4 mW	104 mW	4100 W	**20mW**
Chip Area [6]	3.22 mm^2 ($\lambda^2/40$)	0.715 mm^2 ($\lambda^2/184$)	36 mm^2 ($\lambda^2/3018$)	25mm^2 [1] ($\lambda^2/6400$)	2.16mm^2 ($\lambda^2/66$)	9 mm^2 ($\lambda^2/9579$)	18.5mm^2 ($\lambda^2/1.6\times10^4$)	**0.19mm^2** ($\lambda^2/1.9\times10^6$)

[1] Transmission losses at the center frequency. [2] Transmission losses across the wide bandwidth. [3] Limited by measurement setup. [4] Using an external tuner.
[5] Calculated from measurement plot. [6] λ is the free space wavelength at the center frequency. N/R – Not reported.

Figure 4. (a) Block diagram and chip microphotograph of the implemented 3-port, 8-branch circulator in 65nm CMOS. The switches are modulated at 500MHz, the shunt capacitor in each of the branches is designed to be 2.5pF, and the matching inductor has been realized using the bonding wires connecting the chip to the QFN package, enabling an extremely compact form-factor. The chip occupies an area of 0.19mm^2, representing a miniaturization factor (λ^2/Area) of 2×10^6 at the mid-band frequency of 500MHz. (b) Fractional bandwidth versus miniaturization factor of time-modulated circulator prototypes demonstrated across various implementation platforms such as printed circuit boards, and integrated CMOS and Gallium Nitride (GaN) technologies. (c) Performance comparison of the proposed circulator with prior active circulators, angular momentum biased circulators and switched delay line circulators.

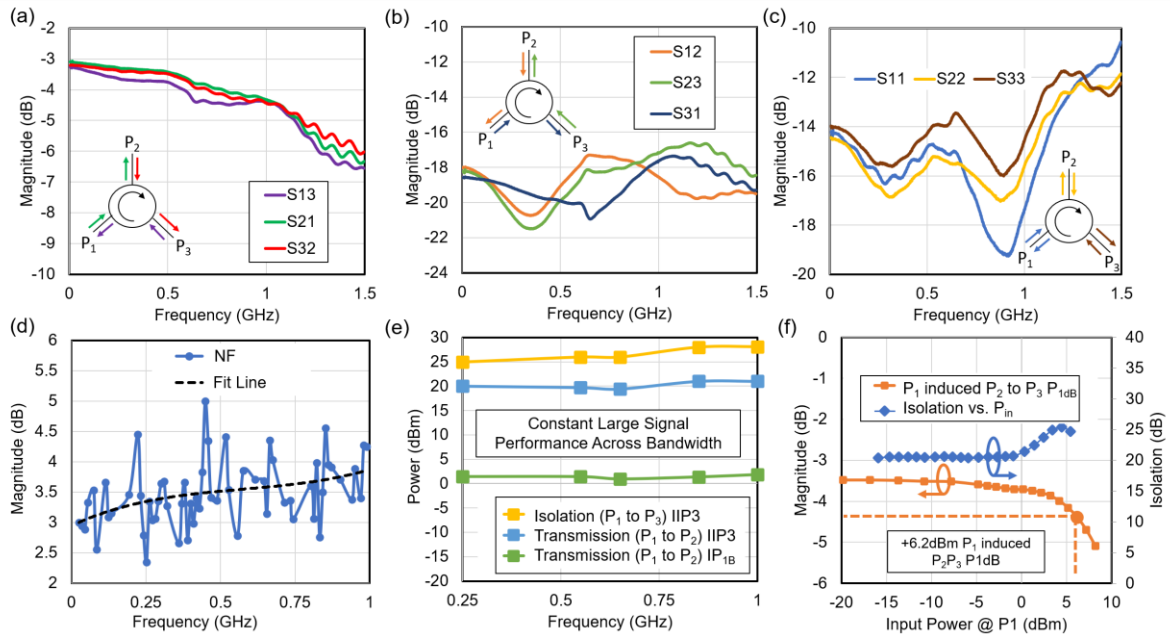


Figure 5. Measured results: (a) transmission scattering parameters in the clockwise direction, (b) isolation scattering parameters in the counterclockwise direction, and (c) matching at all the ports. We observe low loss of 3.1dB - 4.3dB over a wide frequency range of DC – 1GHz. The isolation is between 18dB - 20dB and matching is <-15dB over this frequency range. (d) Noise figure of 3-4dB reveals that the degradation in the signal-to-noise ratio is consistent with the transmission loss, representing negligible effect of the phase noise of the modulation signal. (d) Large-signal performance, namely transmission and isolation IIP3s, and transmission IP1dB. (e) P_1-induced P_2-P_3 compression and isolation compression across input power.

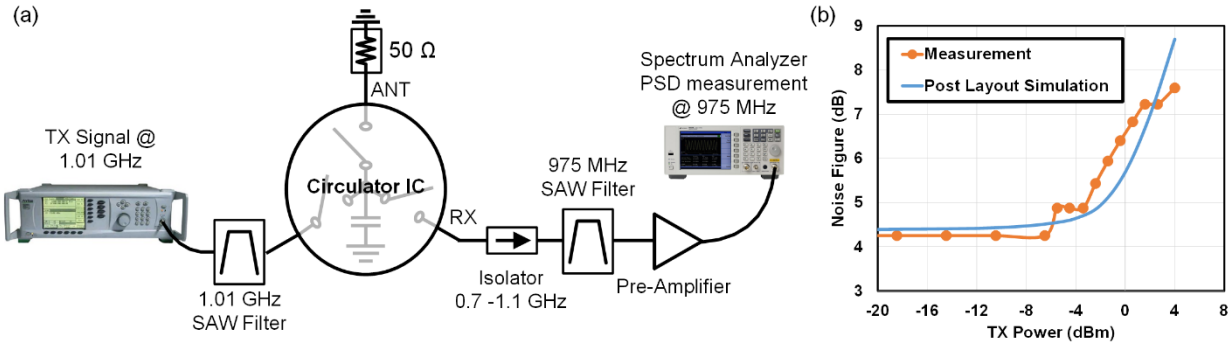


Figure 6. Noise figure from port 2 – port 3 in presence of a strong input signal incident at port 1. (a) Measurement setup. (b) Comparision of the measured performance with simulations.